This paper describes objective technical results and analysis. Any subjective views or opinions that might be expressed in the paper do not necessarily represent the views of the U.S. Department of Energy or the United States Government.

SAND2023-08640J

Molecular-gas-dynamics simulations of turbulent Couette flow over a mean-free-path-scale permeable substrate

Ryan M. McMullen[1], Michael C. Krygier[2], John R. Torczynski[1], and Michael A. Gallis[1]

[1]*Engineering Sciences Center, Sandia National Laboratories, P. O. Box 5800, Albuquerque, New Mexico 87185-0840, USA*

[2]*Center for Computing Research, Sandia National Laboratories, P. O. Box 5800, Albuquerque, New Mexico 87185-0828, USA*

We report flow statistics and visualizations from molecular-gas-dynamics simulations using the direct simulation Monte Carlo (DSMC) method for turbulent Couette flow in a minimal domain where the lower wall is replaced by an idealized permeable fibrous substrate representative of thermal-protection-system materials for which the Knudsen number is $O(10^{-1})$. Comparisons are made with smooth-wall DSMC simulations and smooth-wall direct numerical simulations (DNS) of the Navier-Stokes equations for the same conditions. Roughness, permeability, and noncontinuum effects are assessed. In the range of Reynolds numbers considered herein, the scalings of the skin friction on the permeable substrate and of the mean flow within the substrate suggest that they are dominated by viscous effects. While the regenerative cycle characteristic of smooth-wall turbulence remains intact for all cases considered, we observe that the near-wall velocity fluctuations are modulated by the permeable substrate with a wavelength equal to the pore spacing. Additionally, the flow within the substrate shows significant rarefaction effects, resulting in an apparent permeability that is 13% larger than the intrinsic permeability. In contrast, the smooth-wall DSMC and DNS simulations exhibit remarkably good agreement for the statistics examined, despite the Knudsen number based on the viscous length scale being as large as $O(10^{-1})$. This latter result is at variance with classical estimates for the breakdown of the continuum assumption and calls for further investigations into the interaction of noncontinuum effects and turbulence.

I. INTRODUCTION

Thermal-protection-system (TPS) materials used to coat the surfaces of reentry vehicles are often fibrous and may ablate due to extreme heating rates [1-3], resulting in a rough and permeable surface layer. This surface layer, or "substrate" (not to be confused with the metallic backing on which TPS materials are typically deposited), has the potential to significantly alter the turbulent boundary layer over the vehicle and thereby alter the heating rate and vibrational loading, which could in turn affect vehicle performance. Consequently, the ability to make accurate predictions about turbulent flows over such TPS materials is of great interest.

Turbulent flows over rough surfaces are ubiquitous in both engineering and nature, and, consequently, a vast amount of work has been performed over the last century with the aim of better understanding these flows and improving engineering predictions for them [4-6]. Additionally, significant interest in turbulent flows over permeable surfaces is motivated by their common occurrence in heat exchangers, nuclear reactors, forest canopies, and riverbeds [7-11]. However, the length scales associated with the roughness and permeability of typical TPS materials can be on the order of the gas-molecular mean free path [12], which itself may not be small compared to other characteristic flow length scales. Therefore, in the context of flow over reentry vehicles coated with TPS materials, the validity of predictions from conventional continuum computational fluid dynamics needs to be assessed.

On the other hand, the direct simulation Monte Carlo (DSMC) method of molecular gas dynamics is suitable for flows for which the continuum assumption breaks down. DSMC simulates gas flows by tracking large numbers of computational particles (each of which in turn represents large numbers of gas molecules) that move, collide with each other, and reflect from solid surfaces just like real gas molecules do [13,14]. Because DSMC is a molecular-level method and thus computationally intense, DSMC simulations of near-continuum turbulent flows were not

This article has been authored by an employee of National Technology & Engineering Solutions of Sandia, LLC under Contract No. DE-NA0003525 with the U.S. Department of Energy (DOE). The employee owns all right, title and interest in and to the article and is solely responsible for its contents. The United States Government retains and the publisher, by accepting the article for publication, acknowledges that the United States Government retains a non-exclusive, paid-up, irrevocable, world-wide license to publish or reproduce the published form of this article or allow others to do so, for United States Government purposes. The DOE will provide public access to these results of federally sponsored research in accordance with the DOE Public Access Plan https://www.energy.gov/downloads/doe-public-access-plan.

computationally feasible. However, due to algorithmic and computing-power advances, DSMC has recently been shown to be able to simulate turbulent flows accurately, reproducing known features of decaying turbulence [15,16] and self-sustaining wall-bounded turbulence [13]. Furthermore, DSMC inherently includes noncontinuum effects, such as Knudsen layers adjacent to solid surfaces and molecular thermal fluctuations, which become significant in the dissipation range of the turbulent energy cascade [17-20].

With these capabilities, DSMC is a physically appropriate method for performing high-fidelity simulations to investigate noncontinuum effects in turbulent flows over complex TPS-like rough and permeable substrates. To study these effects, we perform DSMC simulations of minimal Couette flow [21], in which the lower wall has been replaced by an idealized permeable structure with length scales comparable to the porosity length scales of common fibrous TPS materials. To quantify the effects of the permeable substrate, we compare these permeable-wall results from DSMC simulations to corresponding smooth-wall results from DSMC simulations and from direct numerical simulations (DNS) of the Navier-Stokes equations. While DSMC has previously been used to investigate rarefied flow through fibrous TPS materials [2,3,12,22-24], to the best of our knowledge, the present study is the first time noncontinuum effects have been considered for turbulent flow over a permeable wall.

II. SIMULATION DETAILS

The permeable substrate is composed of circular cylinders aligned with the streamwise (x), wall-normal (y), and spanwise (z) directions. Fig. 1 shows a schematic diagram of the flow geometry, along with a detailed view of the cylinder structure. The domain extent is $(L_x, L_y, L_z) = (1.75\pi h, 2h + h_c, 1.2\pi h)$. The free-channel half-height is $h = 500\ \mu\text{m}$, and the cylinder radii, the separation between adjacent cylinders, and the substrate height are $r = 18.7\ \mu\text{m}$, $s = r/10 = 1.87\ \mu\text{m}$, and $h_c = 549.78\ \mu\text{m}$ (i.e., 14 layers), respectively. The resulting porosity is $\varepsilon = 1 - (V_c / L_x L_z h_c) = 0.47$, where V_c is the total volume occupied by all cylinders. The boundary conditions are periodic in the x and z directions, and all solid surfaces are fully-accommodating: reflected gas molecules have a velocity distribution function in equilibrium with the wall [13,14].

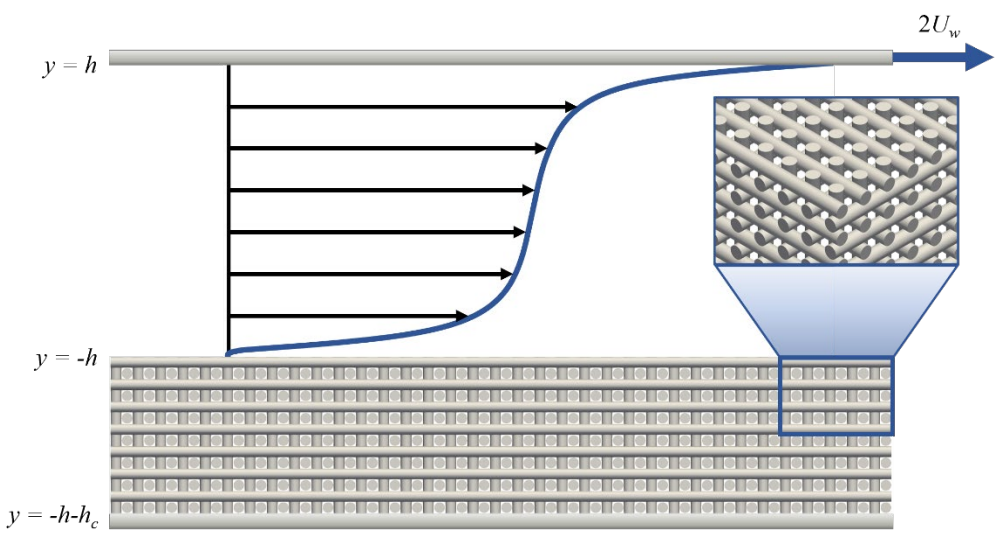

Fig. 1. Schematic diagram of the flow configuration. The inset shows a close-up view of the cylinder structure.

Four different cases, identified by Reynolds number, are considered. Here, the global Reynolds number is defined as $\text{Re}_h = \rho_b U_w h / \mu_w$, where $\rho_b = 0.32\ \text{kg m}^{-3}$ is the bulk, i.e., volume-averaged, density, U_w is half the velocity difference between the upper wall and the cylinder structure, as illustrated in Fig. 1, and $\mu_w = 2.96 \times 10^{-5}\ \text{kg m}^{-1}\ \text{s}^{-1}$ is the value of the dynamic viscosity at the constant temperature $T_w = 273.15\ \text{K}$ of the walls and cylinders. The global Mach number is defined as $\text{Ma} = U_w / a_w$, where $a_w = \sqrt{\gamma k_\text{B} T_w / m}$ is the sound speed at the wall temperature, $\gamma = 5/3$ is the specific heat ratio, k_B is the Boltzmann constant, and $m = 6.63 \times 10^{-26}\ \text{kg}$ is the molecular mass. The

global Mach and Reynolds numbers are varied by changing the value of U_w. Consequently, the global Knudsen number for all cases is $\mathrm{Kn}_h = \lambda_b / h = \sqrt{\pi\gamma / 2}\,\mathrm{Ma} / \mathrm{Re}_h = 9.7\times10^{-4}$, where λ_b is the molecular mean free path based on ρ_b and T_w. For comparison with the permeable-wall simulations, corresponding smooth-wall DSMC simulations, in which the cylinder structure is replaced by a smooth impermeable wall located at $y = -h$, are also performed for the same conditions. A summary of the conditions for the simulations is provided in Table 1.

Here, we define the notation that will be used throughout the remainder of the text. Velocities and length scales normalized by U_w and h, respectively, are referred to as being in outer units or as outer-scaled. When referring to the permeable-wall simulations, quantities evaluated at the top of the cylinder structure ($y = -h$) and the upper wall ($y = h$) are denoted by superscripts l and u, respectively. For the smooth-wall simulations, the distinction between upper and lower walls is not made due to symmetry. Velocities and length scales normalized by the friction velocity $u_\tau^{u/l} = \sqrt{\tau^{u/l} / \rho^{u/l}}$ and viscous length scale $\mu_w / \rho^{u/l} u_\tau^{u/l}$, respectively, are referred to as being in inner units or as inner-scaled and are denoted with a superscript $+$. In cases where this notation is ambiguous, the explicit definition of the quantity is provided.

The DSMC simulations are performed using Sandia's open-source large-scale code SPARTA [25,26]. The permeable-wall and smooth-wall domains are divided into $N_x \times N_y \times N_z = 1982\times1118\times1360$ and $N_x \times N_y \times N_z = 1982\times722\times1360$ uniform cells, respectively. For the conditions considered herein, this cell size yields a mean collision separation comparable to λ_b, such that any potential shocks will be well-resolved. Note that this resolution requirement is much more stringent than any imposed by the turbulence. The simulations use 30 particles per cell on average, giving approximately 73 billion particles total, where each particle represents 428438 real gas molecules. The time step is 4.56×10^{-11} s for the $\mathrm{Re} = 500$, 1000, and 1500 cases and 1.14×10^{-11} s for the $\mathrm{Re} = 2000$ case, which is $\approx 1\%$ of the mean collision time. Particle-particle collisions are performed using the variable-soft-sphere (VSS) interaction, which produces a viscosity temperature dependence of the form $\mu(T) = \mu_w (T / T_w)^\omega$, with $\omega = 0.81$ [14]. The DSMC simulations were performed on 1000 nodes of the Lawrence Livermore National Laboratories Sierra supercomputer, each node having four NVIDIA Volta V100 GPUs. The simulations advanced approximately two million moves per 24 hours and were run to at least 70 million moves.

For the permeable-wall simulations, a cut-cell method is used to conform the mesh to the cylinder structure [25]. In this approach, a closed three-dimensional surface, represented by triangular surface elements, is embedded in the Cartesian grid. The surface elements intersecting a given grid cell reduce (or cut) the portion of its volume accessible to particles, and the reduced volume for each cut cell is then calculated and taken into account when performing particle-particle collisions. The particles are initially distributed uniformly over all uncut cells in the domain. Since the only cut cells are within the cylinder structure, there is an initial rapid net motion of particles from the free portion of the channel into the cylinder structure.

Velocity fields from the DSMC simulations are obtained by averaging over the particles contained within each cell. However, since each simulated particle represents many real molecules, the statistical variations arising from thermal molecular fluctuations is drastically overestimated [14,17], often resulting in an unacceptably low signal-to-noise ratio. A common technique to mitigate this effect is to additionally perform temporal averaging of the molecules. That is, each velocity field is obtained from the average over many time steps. Ideally, an averaging time that gives acceptable noise reduction is still much smaller than any macroscopic flow time scale, though this is not always possible. Here, we found that it was necessary to average over a time window of 10^5 time steps, which is comparable to the convective time scale L_x / U_w. This precludes computing accurate turbulent velocity fluctuation statistics, such as the Reynolds stresses, across the majority of the free portion of the channel. However, since the permeable-wall DSMC simulations are performed in the reference frame in which the lower wall is stationary (see Fig. 1), this averaging effect is minimal close to the cylinder structure. Furthermore, we have compared the results pertaining to near-wall turbulent velocity fluctuations presented in Section III-C with a limited data set using an averaging time two orders of magnitude smaller to confirm that the conclusions drawn herein are not significantly influenced by averaging effects.

We remark that variance-reduced DSMC [27,28] can be used to reduce statistical uncertainty in hydrodynamic quantities. However, this method is more efficient than the standard DSMC method only for low-speed flows ($\mathrm{Ma} \lesssim 0.1$) [27] and was thus not used in the present work.

In addition to the DSMC simulations, continuum direct numerical simulations (DNS) of smooth-wall Couette flow for the same flow conditions using the Sandia-developed shock-capturing finite volume code SPARC [29] are performed in order to distinguish any noncontinuum effects from the impact of the cylinder structure on the turbulence. SPARC utilizes the high-order-accurate Subbareddy-Candler scheme [30] in smooth regions of the flow and applies modified Steger-Warming fluxes [31] in regions of the flow where large Mach-number-gradients are detected. Time is advanced using a fourth-order explicit Runge-Kutta scheme with a Courant-Friedrichs-Lewy number of 0.5 to determine the time step.

The DNS are performed using grids of $N_x = N_y = N_z = 128$ for the $\mathrm{Re} = 500$ case and $N_x = N_y = N_z = 192$ for the $\mathrm{Re} = 1000$, 1500, and 2000 cases. Uniform grid spacing is used in the homogeneous wall-parallel directions x and z, resulting in $\Delta x^+ \le 4.9$ and $\Delta z^+ \le 2.7$ for all cases, and the grid in the wall-normal direction is stretched using a hyperbolic tangent distribution, such that the near-wall resolution is $\Delta y^+_{\min} \le 0.27$ and the resolution at the channel center is $\Delta y^+_{\max} \le 2.7$ for all cases. The present simulations thus have resolutions comparable to other DNS studies of compressible wall-bounded turbulence [30,32-37]; resolution comparisons with channel flow are included because there are few DNS studies of compressible turbulent Couette flow [35-39]. Additionally, comparison with $\mathrm{Re} = 1000$, 1500, and 2000 simulations using $N_x = N_y = N_z = 128$ grids confirms that all statistics reported herein are well-converged. As in the DSMC simulations, the boundary conditions are periodic in the x and z directions. However, in contradistinction to the DSMC simulations, the no-slip condition is imposed at the two isothermal walls. The DNS cases are summarized in Table 1.

DNS of the permeable-wall geometry is not performed since, as we demonstrate in Section IV-B, the relatively large values of the pore-scale Knudsen number prevent continuum simulations from accurately capturing the apparent permeability of the cylinder structure [40]. Indeed, even the Navier-Stokes equations with velocity-slip/temperature-jump boundary conditions become inaccurate for Knudsen numbers $\gtrsim 10^{-1}$ [41]. Additionally, from a practical perspective, meshing the cylinder structure poses significant challenges. The cell size required to produce a cylinder-structure mesh of sufficient quality is a fraction of the cylinder spacing; we estimate this would produce a mesh with billions of cells, making such simulations unwieldy. Other avenues that could potentially circumvent the meshing issues, such as using an immersed-boundary method, still suffer the same fundamental limitations of physical validity discussed above and, therefore, were not pursued for the present work. Consequently, the primary purpose of the smooth-wall DNS is to serve as a point of comparison for the smooth-wall DSMC simulations. Finally, we note that, by contrast, meshing complex geometries like the cylinder structure considered herein is trivial for DSMC simulations.

Because of the averaging effects discussed above for the DSMC simulations, standard measures of compressibility effects, such as the turbulent Mach number $\mathrm{Ma}_t = u_{\mathrm{rms}} / \bar{a}$, where $u_{\mathrm{rms}} = \sqrt{\overline{u'^2} + \overline{v'^2} + \overline{w'^2}}$ is the rms fluctuating velocity and $\bar{a}$ is the mean sound speed, will be underestimated. Therefore, the DNS was also used to assess compressibility effects. As shown in Appendix A, even for the highest-Mach-number case ($\mathrm{Ma} = 1.2$), the turbulent Mach number is everywhere less than 0.22, indicating that compressibility effects beyond mean property variation on the turbulence statistics are minor [42]. Furthermore, no shocklets were observed in any of the velocity fields examined. Consequently, compressibility effects are not a focus of the present work.

The initial condition for all simulations is the incompressible laminar smooth-wall solution $u = U_w(y/h + 1)$ plus a sinusoidal perturbation with amplitude sufficient to trigger transition to turbulence. All simulations remained turbulent, with the exception of the $\mathrm{Re} = 500$ permeable-wall DSMC case, which rapidly relaminarized. This latter behavior is unsurprising, given that $\mathrm{Re} = 500$ is near the threshold for which turbulence first appears in minimal Couette flow [21] and that turbulent Couette flow has a finite lifetime [43], even at higher Re. However, a second $\mathrm{Re} = 500$ simulation did remain turbulent, and results from this second run are reported herein. For reference, the shear stress from the run that relaminarized is also shown in Fig. 2(a).

For all simulations, statistics are collected for $tU_w / h > 200$ to allow the flow to reach statistically steady state, which is confirmed by examination of the skin friction shown in Figs. 2 and 3 and is consistent with previous work [13]. As shown in Appendix B, we additionally confirm for the permeable-wall DSMC simulations that the density within the cylinder structure reaches statistically steady state by this time. Subsequently, DSMC realizations were collected every 10^6 time steps, giving at least 45 realizations for all cases. The reported statistics are then computed by averaging realizations up to $tU_w / h = 600$. Although running the DSMC simulations for significantly longer times is not feasible, the DNS statistics computed over the same time interval, $200 < tU_w / h < 600$, were

compared to statistics computed over much longer intervals (up to $tU_w / h \approx 5000$) and were found to be in good agreement [13], suggesting that the reported statistics are sufficiently converged.

Table 1. Reynolds, Mach, and Knudsen numbers for all simulation cases. The case labels use the format: simulation type (DSMC / DNS)-wall type (P = permeable / S = smooth) Re_h .

Case	Re_h	Ma	Kn_h
DSMC-P500	500	0.3	9.7×10^{-4}
DSMC-P1000	1000	0.6	
DSMC-P1500	1500	0.9	
DSMC-P2000	2000	1.2	
DSMC-S500	500	0.3	9.7×10^{-4}
DSMC-S1000	1000	0.6	
DSMC-S1500	1500	0.9	
DSMC-S2000	2000	1.2	
DNS-S500	500	0.3	0
DNS-S1000	1000	0.6	
DNS-S1500	1500	0.9	
DNS-S2000	2000	1.2	

III. RESULTS

A. Skin friction

Here, we examine the time-resolved skin friction across the different cases and simulation sets. Fig. 2 shows a comparison of the upper-wall shear stress τ^u for the smooth-wall DNS, smooth-wall DSMC, and permeable-wall DSMC simulations. The mean and root-mean-square (rms) values are reported in Table 2. For all four Reynolds numbers, the mean values and fluctuations are very similar for all three simulation sets, suggesting the cylinder structure has little influence on the upper-wall shear stress. Except for $\mathrm{Re} = 500$, the smooth-wall DSMC simulations show a larger initial overshoot than the permeable-wall simulations and are more comparable to the DNS. Also shown in Fig. 2(a) is the upper-wall shear stress from the first permeable-wall $\mathrm{Re} = 500$ DSMC run discussed in Section II, which reaches the laminar shear stress value $\tau_{\mathrm{lam}} h / \mu_w U_w = 1$ by $tU_w / h \approx 400$.

For the permeable-wall DSMC simulations, we define the lower-wall skin friction as the total streamwise force on the cylinder structure F_x per unit horizontal area, i.e., $\tau^l = F_x / L_x L_z$. This definition is consistent with rough-wall turbulence experiments which directly measure surface drag using a drag balance [6] and has also recently been used in permeable-wall experiments [44]. In Fig. 3, we compare the lower-wall skin friction with the upper-wall shear stress; the mean and rms values are also reported in Table 2. Except for the $\mathrm{Re} = 500$ case, the streamwise cylinder force shows a significantly larger initial overshoot than the upper-wall shear stress. This overshoot is possibly explained by the flow initially driving particles into the cylinder structure as the steady-state density profile in the channel is established. The fluctuations in the upper-wall shear stress and lower-wall skin friction are strongly correlated for all four Reynolds numbers, implying the presence of flow structures that span the entirety of the free portion of the channel, which is a common feature of smooth-wall plane Couette flow [45].

Additionally, the upper- and lower-wall friction velocities $u_\tau^{u/l}$ and friction Reynolds numbers $\mathrm{Re}_\tau^{u/l} = \rho^{u/l} u_\tau^{u/l} h / \mu_w$ are reported in Table 2. For all cases, the permeable-wall values differ by at most a few percent from the corresponding smooth-wall DSMC and DNS values.

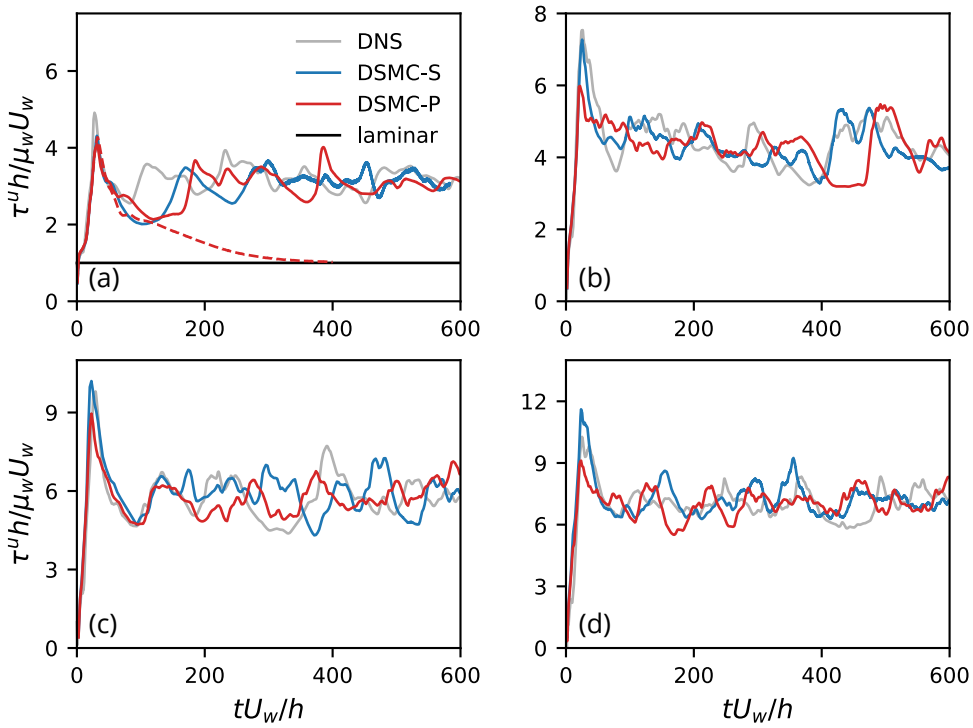

Fig. 2. Comparison of shear stress on the upper wall from the smooth-wall DNS and smooth-wall and permeable-wall DSMC simulations. (a) Re = 500, (b) Re = 1000, (c) Re = 1500, (d) Re = 2000. The dashed line in (a) is from the first permeable-wall DSMC Re = 500 run, and the black line is the laminar value of the shear stress.

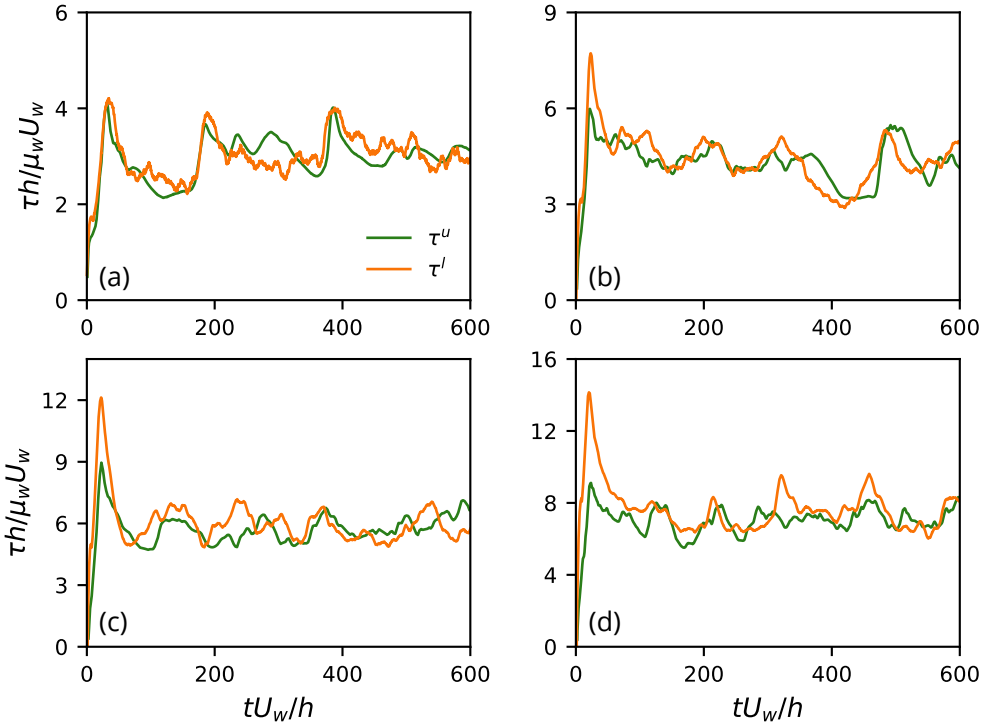

Fig. 3. Comparison of upper- and lower-wall skin friction from the permeable-wall DSMC simulations. (a) Re = 500, (b) Re = 1000, (c) Re = 1500, (d) Re = 2000.

Table 2. Skin friction, friction velocities, and friction Reynolds numbers for all cases. For the permeable-wall DSMC simulations, quantities evaluated for the upper and lower walls are denoted with superscripts ^{u} and ^{l}, respectively. Skin friction is reported in the format mean ± rms.

Case	$\tau^u h / \mu_w U_w$	$\tau^l h / \mu_w U_w$	u_τ^u [m s^{-1}]	u_τ^l [m s^{-1}]	Re_τ^u	Re_τ^l
DSMC-P500	3.11 ± 0.26	3.10 ± 0.31	7.26	7.23	39.7	39.6
DSMC-P1000	4.22 ± 0.59	4.19 ± 0.60	11.7	11.7	66.6	67.1
DSMC-P1500	5.76 ± 0.54	5.85 ± 0.59	16.2	16.2	99.3	100
DSMC-P2000	7.12 ± 0.49	7.42 ± 0.84	19.9	20.1	132	136
DSMC-S500	3.18 ± 0.20		7.32		40.2	
DSMC-S1000	4.19 ± 0.47		11.8		68.4	
DSMC-S1500	5.67 ± 0.63		15.8		101	
DSMC-S2000	7.24 ± 0.58		19.4		138	
DNS500	3.21 ± 0.28		7.26		39.9	
DNS1000	4.21 ± 0.53		11.6		67.4	
DNS1500	5.75 ± 0.76		15.8		100	
DNS2000	7.00 ± 0.65		19.3		137	

B. Mean velocity profiles

Next, we analyze the mean velocity profiles for the different simulations. Fig. 4 compares the mean velocity profiles scaled in outer units from the smooth-wall DNS, smooth-wall DSMC, and permeable-wall DSMC simulations for all four Reynolds numbers. The permeable-wall profiles are split into lower and upper halves, and the velocity at the corresponding wall has been subtracted, i.e., the quantity plotted in Fig. 4 is $|U(y) - U(\pm h)|/U_w$. $U(h) = 2U_w$ is the velocity of the upper wall, while $U(-h) = U_{\mathrm{slip}}$ is the slip velocity at the permeable cylinder structure interface; for this reason, the upper and lower profiles plotted in this manner are not expected to agree at the channel center. The profiles are plotted against the outer-scaled distance from the corresponding wall: $|y \pm h|/h$.

In all cases, the smooth-wall DNS and smooth-wall DSMC profiles agree well. For $\mathrm{Re} = 500$, the upper and lower permeable-wall profiles are also in good agreement with the smooth-wall results, indicating that there is no significant impact of the cylinder structure on the mean velocity profile for this case. For higher values of Re, the upper permeable-wall profiles continue to agree well with the smooth-wall profiles, while the discrepancy due to the interface slip velocity in the lower permeable-wall DSMC profile increases. However, this discrepancy does not increase monotonically with Re and is largest for the $\mathrm{Re} = 1500$ case.

This latter observation can be explained by comparing the permeable-wall DSMC mean velocity profiles across the entire free portion of the channel, as is shown in Fig. 5. As expected, the near-wall gradients increase with increasing Re. However, the profiles for the higher Re values show notable departures from the antisymmetry expected for smooth-wall Couette flow. This can be seen more clearly in Fig. 5(b), which shows a zoomed-in view of the profiles in the center region of the channel. The $\mathrm{Re} = 500$ and 1000 cases have local maxima and minima at $y/h \approx \pm 0.25$ due to channel-spanning streamwise rolls that redistribute streamwise momentum [46] and are consistent with previous observations of low-Re minimal Couette turbulence [21]. The trend of the profiles in the region $-0.5 \lesssim y/h \lesssim 0$ is nonmonotonic with increasing Re; the mean velocity in this region first decreases with increasing Re for $\mathrm{Re} = 500\text{-}1500$ but subsequently increases for $\mathrm{Re} = 2000$. This latter increase is consistent with higher-Re Couette turbulence [47] and explains the larger discrepancy between the lower-half and upper-half permeable-wall DSMC profiles for $\mathrm{Re} = 1500$ in Fig. 4.

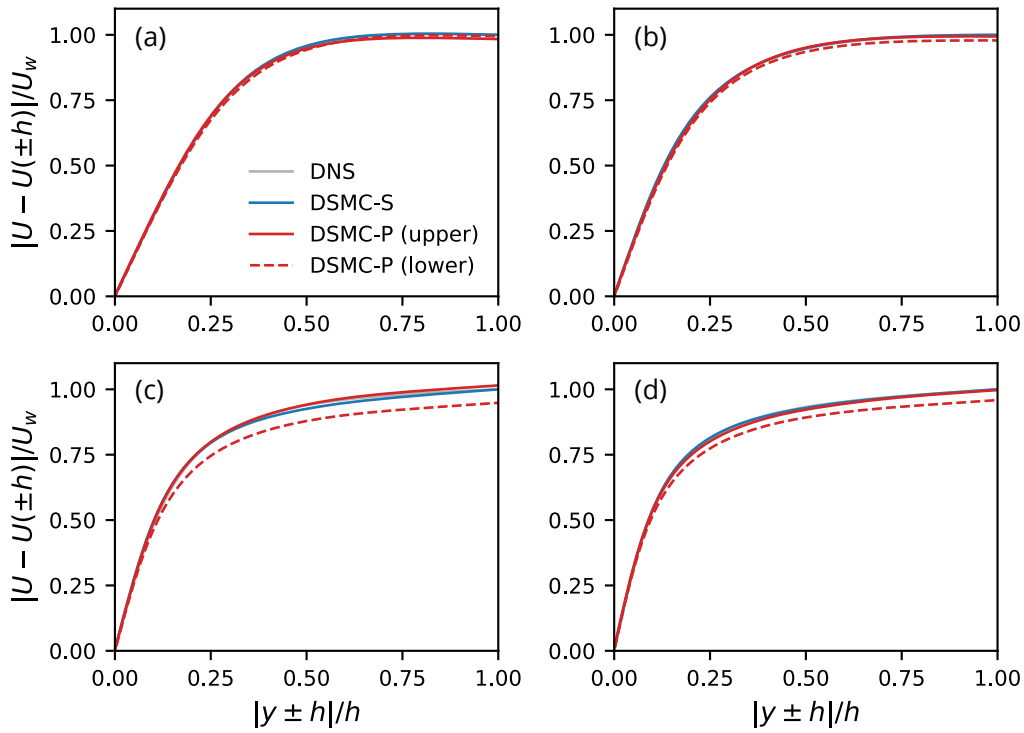

Fig. 4. Mean velocity profiles from the smooth-wall DNS and smooth-wall and permeable-wall DSMC simulations plotted against distance from the appropriate wall. (a) Re = 500, (b) Re = 1000, (c) Re = 1500, (d) Re = 2000.

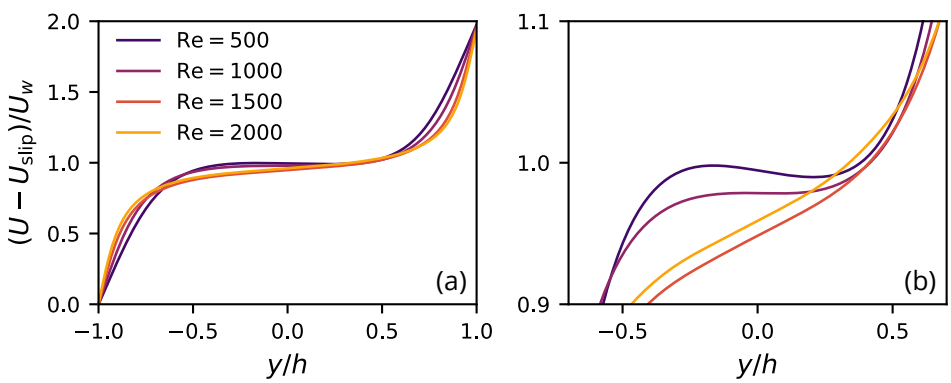

Fig. 5. Permeable-wall DSMC mean velocity profiles (a) across the entire free portion of the channel and (b) zoomed in on the central region of the channel.

We also examine the mean profiles scaled in inner units. Fig. 6 compares the inner-scaled DNS, permeable-wall DSMC, and smooth-wall DNS mean velocity profiles. Here again, the permeable-wall DSMC profiles are split into lower and upper halves, and the interface slip velocities are subtracted from the lower-half profiles. The upper and lower profiles are normalized by u_τ^u and u_τ^l, respectively. The profiles are plotted against $y^+ = \rho^{u/l} u_\tau^{u/l} \,|\, y \pm h \,|\, / \mu_w$. For $\mathrm{Re} = 500$ and 1000, both the lower and upper profiles are nearly identical to the smooth-wall case, with only a slight difference becoming apparent above the buffer layer for $\mathrm{Re} = 1000$. By contrast, the effects of the permeable structure are clearly visible in the lower half of the channel for the two highest Reynolds numbers. For $\mathrm{Re} = 1500$, there is a significant velocity deficit on the cylinder side across the majority of the boundary layer. Nonetheless, the upper-half profile is still essentially unchanged from the smooth-wall case. On the other hand, for $\mathrm{Re} = 2000$, both

the upper- and lower-half exhibit a clear deficit relative to the smooth-wall case for $y^+ \gtrsim 15$, indicating that the effects of the cylinder structure extend across the majority of the channel for this case.

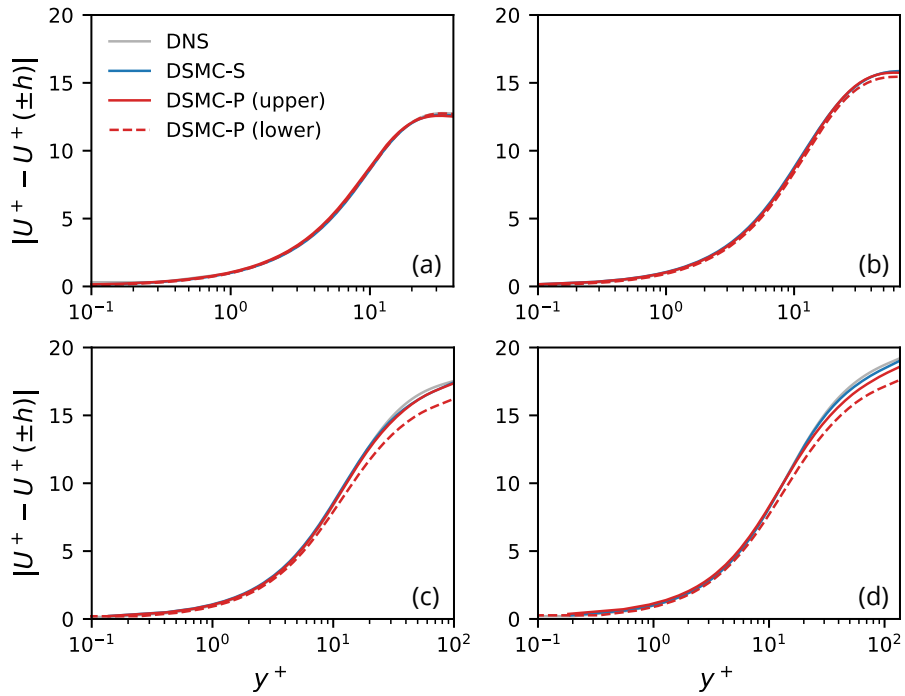

Fig. 6. Inner-scaled mean velocity profiles from the smooth-wall DNS and smooth-wall and permeable-wall DSMC simulations. (a) Re = 500, (b) Re = 1000, (c) Re = 1500, (d) Re = 2000.

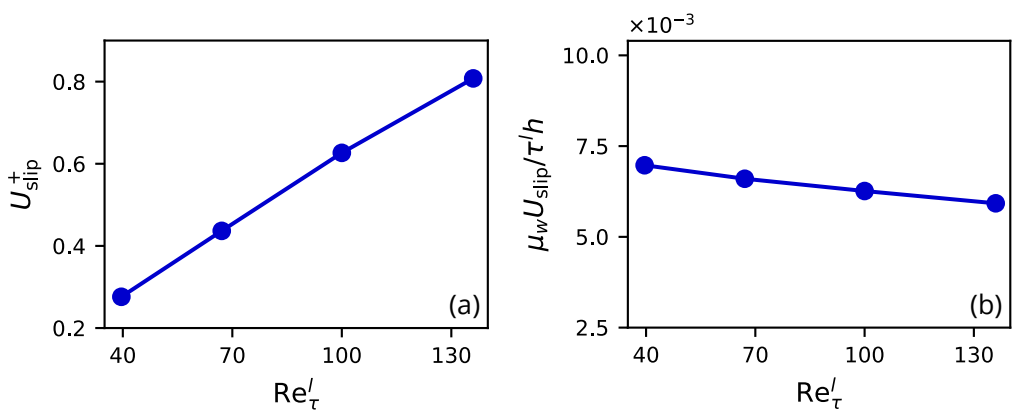

Fig. 7. Interface velocity U_{slip} normalized by (a) u^l_τ and (b) $\tau^l h / \mu_w$ as functions of Re^l_τ.

Next, we comment on the slip velocity at the cylinder structure interface. As shown in Fig. 7(a), $U^+_{\mathrm{slip}} = U_{\mathrm{slip}} / u^l_\tau$ increases approximately linearly with Re^l_τ over the modest range considered herein. This implies the approximate scaling $U_{\mathrm{slip}} \sim \tau^l h / \mu_w$. To verify this, we plot $\mu_w U_{\mathrm{slip}} / \tau^l h$ in Fig. 7(b), which, although not strictly constant, varies only weakly with Re^l_τ over the same range. On the other hand, observations from experiments and simulations conducted at higher Reynolds numbers suggest that either $U_{\mathrm{slip}} / U_e \approx 0.3$ [48,49], where U_e is the boundary layer edge velocity, or $U^+_{\mathrm{slip}} \approx 3-5$ [44]. However, the extant data in the literature is not sufficient to discriminate between these two scalings. Nonetheless, both are distinct from the scaling demonstrated in Fig. 7, which suggests a transition

at some intermediate Reynolds number. Indeed, Suga et al. [50] observed a rapidly increasing U_{slip} for low Reynolds numbers, followed by saturation at higher Reynolds numbers. Here, we propose that this change in behavior can be rationalized by noting that the present scaling, $\tau^l \sim \mu_w U_{\text{slip}} / h$, suggests that the drag on the cylinder structure is dominated by viscosity, while the scaling $U_{\text{slip}} \sim u_\tau^l$, or, rearranging, $\tau^l \sim \rho^l U_{\text{slip}}^2$, suggests that pressure drag dominates, as is the case for flow over rough surfaces in the fully rough regime [6].

Finally, we examine the behavior of the mean flow within the cylinder structure. Fig. 8(a) shows the DSMC mean velocity profiles for all four cases within the top three layers of the cylinder structure normalized by u_τ^l. All cases exhibit a region of reversed flow within the top cylinder layer, the magnitude of which increases with increasing Reynolds number. This pattern is indicative of recirculation vortices similar to those observed in "*d*-type" roughness [51-53]. In the second layer, a similar pattern is observed, albeit with the opposite sign and significantly diminished magnitude. Below the second layer, the mean velocity decays rapidly, suggesting that the flow does not penetrate deeply within the cylinder structure. We also show the mean velocities normalized by $\tau^l h / \mu_w$ in Fig. 8(b), which almost perfectly collapses the profiles in the second layer, indicating that $\tau^l h / \mu_w$ is the relevant velocity scale for the mean flow within the structure. However, the profiles do not perfectly collapse within the first layer, though they do so significantly more than when scaled by u_τ^l (Fig. 8(a)). The failure to totally collapse is unsurprising given the weak Reynolds number dependance observed for $\mu_w U_{\text{slip}} / \tau_\tau^l h$ in Fig. 7(b) and suggests that the interaction with the turbulence in the free portion of the channel introduces a different velocity scale for the interface flow.

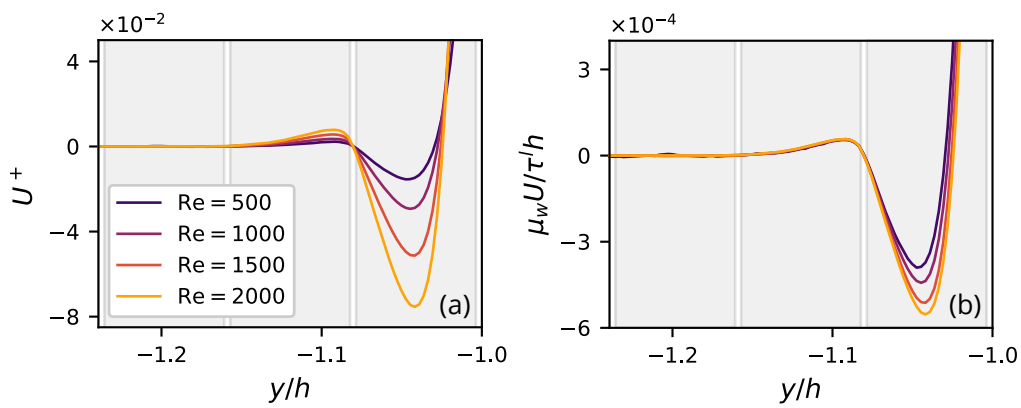

Fig. 8. Permeable-wall DSMC mean velocity profiles zoomed in on the top three layers of the cylinder structure, normalized by (a) u_τ^l and (b) $\tau^l h / \mu_w$. Shaded regions indicate the locations of the cylinder layers.

C. Near-wall velocity fluctuations

To assess the effects of the cylinder structure on the near-wall turbulence, we compare representative snapshots of velocity fluctuations in the plane $y^+ = 5$ from the DNS, smooth-wall DSMC, and permeable-wall DSMC simulations. The permeable-wall DSMC fluctuations are shown on the cylinder side.

For $\text{Re} = 500$, shown in Fig. 9, all three simulations show a single pair of high-speed and low-speed streaks, as expected for minimal Couette turbulence at low Reynolds numbers [13,21]. The fluctuations in the permeable-wall DSMC simulation are essentially identical to the smooth-wall simulations and show no significant influence by the cylinder structure. These qualitative observations are supported by comparison of the premultiplied velocity spectra, e.g., $k_x k_z E_{uu} / u_\tau^{l2}$, where k_x and k_z are the streamwise and spanwise wavenumbers, respectively, which are shown in Fig. 10 in the same wall-normal plane, $y^+ = 5$. All spectra are plotted as functions of the inner-scaled streamwise and spanwise wavelengths $\lambda_x^+ = \rho^l u_\tau^l \lambda_x / \mu_w = 2\pi \rho^l u_\tau^l / k_x \mu_w$ and $\lambda_z^+ = \rho^l u_\tau^l \lambda_z / \mu_w = 2\pi \rho^l u_\tau^l / k_z \mu_w$, respectively. For clarity, only the permeable-wall DSMC and DNS contours are shown; spectra for the smooth-wall DSMC simulations and DNS agree well for all cases. The permeable-wall DSMC and DNS spectra show good agreement for $\text{Re} = 500$, especially in the most energetic regions. There are slight discrepancies for the lower contour levels and large λ_z^+, where the DSMC fluctuations are slightly attenuated relative to the DNS ones. However, this is possibly an artifact of the temporal averaging employed when extracting the DSMC velocity fields, as discussed in Section II.

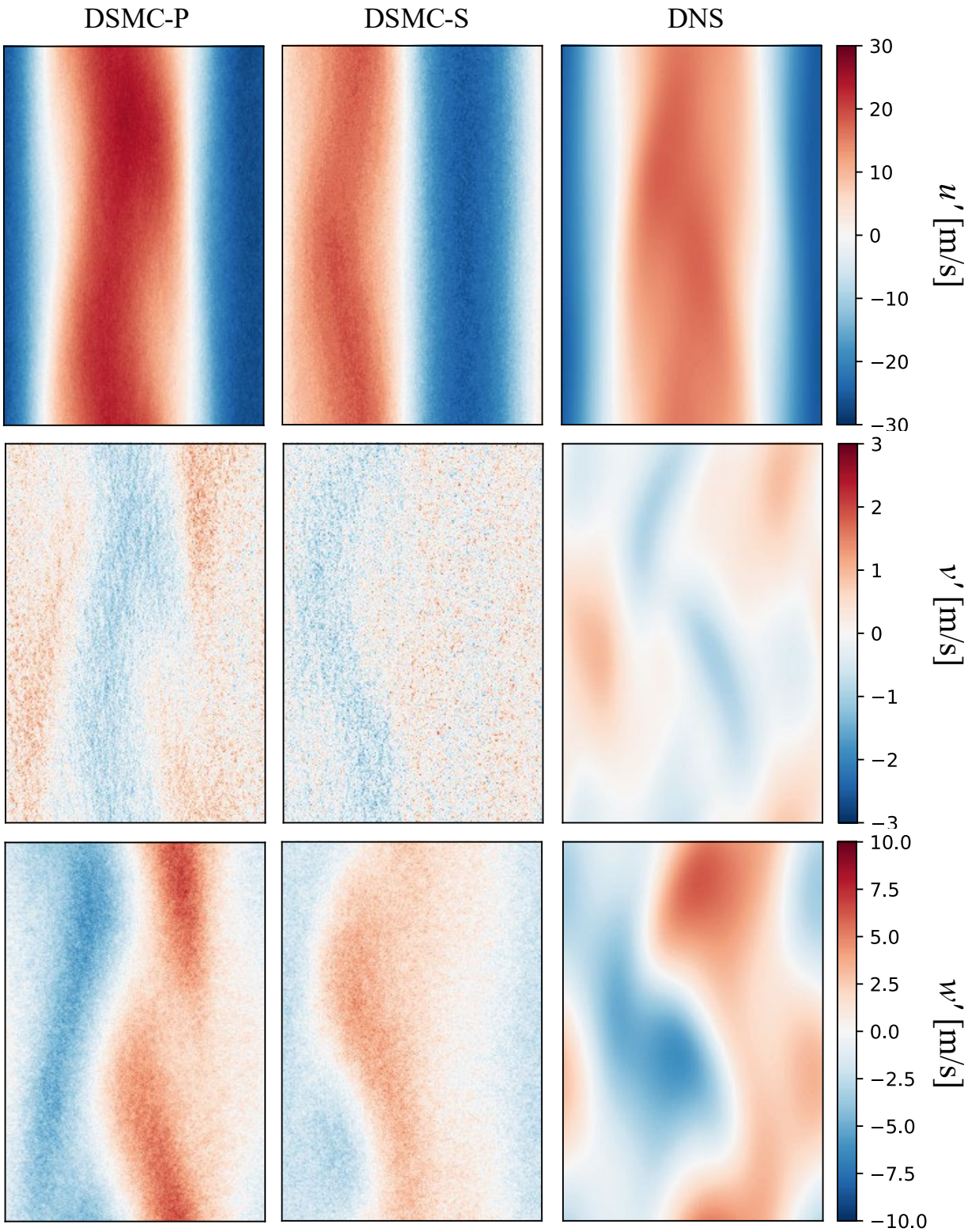

Fig. 9. Comparison of velocity fluctuations for $\mathrm{Re} = 500$ at $y^+ = 5$. Left column: permeable-wall DSMC, center row: smooth-wall DSMC, right column: smooth-wall DNS. Top row: u, center row: v, bottom row: w. Images in the same row have the same color scale.

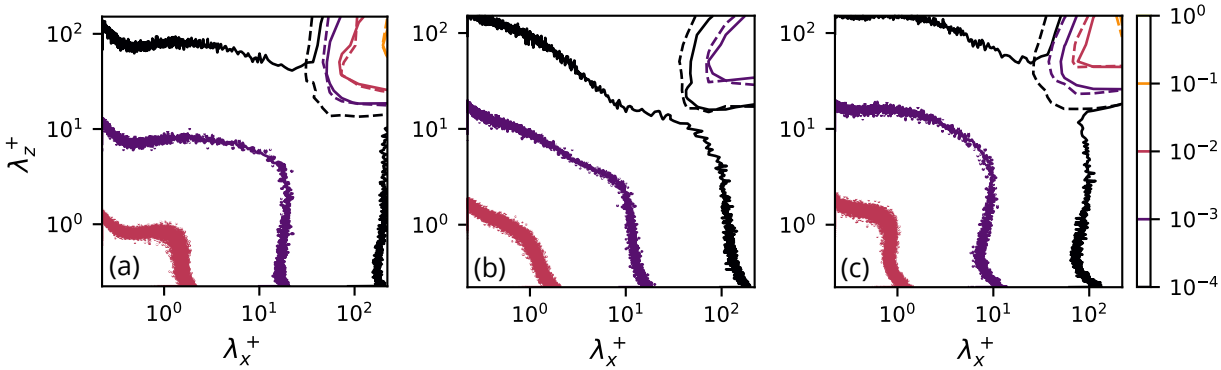

Fig. 10. Premultiplied energy spectra for $\mathrm{Re} = 500$ at $y^+ = 5$. a) $k_x k_z E_{uu} / u_\tau^{l2}$, b) $k_x k_z E_{vv} / u_\tau^{l2}$, c) $k_x k_z E_{ww} / u_\tau^{l2}$. Solid lines are the permeable-wall DSMC. Dashed lines are the DNS.

Additional small-scale fluctuations are visible in the DSMC spectra, which correspond to molecular thermal fluctuations; as discussed in Section II, the magnitude of these fluctuations is exaggerated in these simulations since each computational particle statistically represents many real molecules. Thermal fluctuations have recently been shown to dominate the dissipation range of the energy spectrum in isotropic turbulence [17-20]. Also consistent with observations in isotropic turbulence, they do not appear to have a significant effect on the statistics of the large scales. However, a detailed investigation of the role thermal fluctuations play in wall-bounded turbulence is the subject of future work. Finally, we note that the increase in the thermal-fluctuation magnitude with decreasing wavelength is due to premultiplication by $k_x k_z$ in Fig. 10.

For the higher-Re cases, shown in Figs. 11-13, the velocity fluctuations for all three simulation sets remain qualitatively similar. As in the $\mathrm{Re} = 500$ case, the streamwise velocity fluctuations consist primarily of streaky structures spanning the entire streamwise extent of the domain, though their spanwise wavelengths become progressively smaller with increasing Re. The fact that the permeable-wall and smooth-wall fluctuations remain very similar suggests that the cylinder structure does not significantly disrupt the near-wall regenerative cycle, contrary to observations for flow over very rough [4] or highly permeable [48,54] surfaces. The spectra for the $\mathrm{Re} = 2000$ case, shown in Fig. 14, confirm this observation. The overall shapes of the permeable-wall DSMC and DNS spectra remain largely similar, though substantial enhancement of the wall-normal fluctuations for the permeable-wall DSMC simulation is apparent and is consistent with previous observations [10,48,55].

Unlike the $\mathrm{Re} = 500$ case, the higher-Reynolds-number permeable-wall DSMC simulations exhibit spatially regular small-scale fluctuations in u and v, which are apparent in Figs. 11-13. These fluctuations are due to the presence of the cylinder structure, which is confirmed in Fig. 14. A distinct peak can be observed at $\lambda_x^+ = \lambda_z^+ = 21.4$, which corresponds to the spacing between adjacent vertical cylinders $2(s+2r)$, and several harmonics and subharmonics are also visible; pore-scale fluctuations are also observed by [56]. Though not shown here, the spectral signature of the cylinder structure is also seen in the spectra for the $\mathrm{Re} = 1000$ and 1500 cases. This signature extends to the largest spanwise wavelengths, suggesting organization across the entire width of the channel. While this is reminiscent of the Kelvin-Helmholtz-like roller structures observed in flow over riblets [57,58], vegetation canopies [7,11], varying-phase opposition control [59], and highly permeable substrates [48,51,54,56,60-63], we emphasize that the present pore-scale fluctuations are not related. Indeed, the Kelvin-Helmholtz-like rollers have much larger streamwise wavelengths $\lambda_x^+ \approx 100-200$ [57,61] than the present pore-scale fluctuations. Moreover, the presence of roller structures typically corresponds to eradication of the smooth-wall regenerative cycle and a substantial drag increase [48], whereas we observe herein only a modest modulation of the smooth-wall fluctuations and negligible drag increase relative to the smooth-wall cases.

Finally, we do not observe any spectral signature indicative of the secondary flows that develop within riblet grooves, i.e., streamwise-elongated structures [57]. This is unsurprising given that the vertical cylinders protrude above the top streamwise-aligned cylinder layer by $\lesssim 0.5$ viscous units (see Table 3) and that the gaps between rows of vertical cylinders presumably inhibit the formation of such secondary flows.

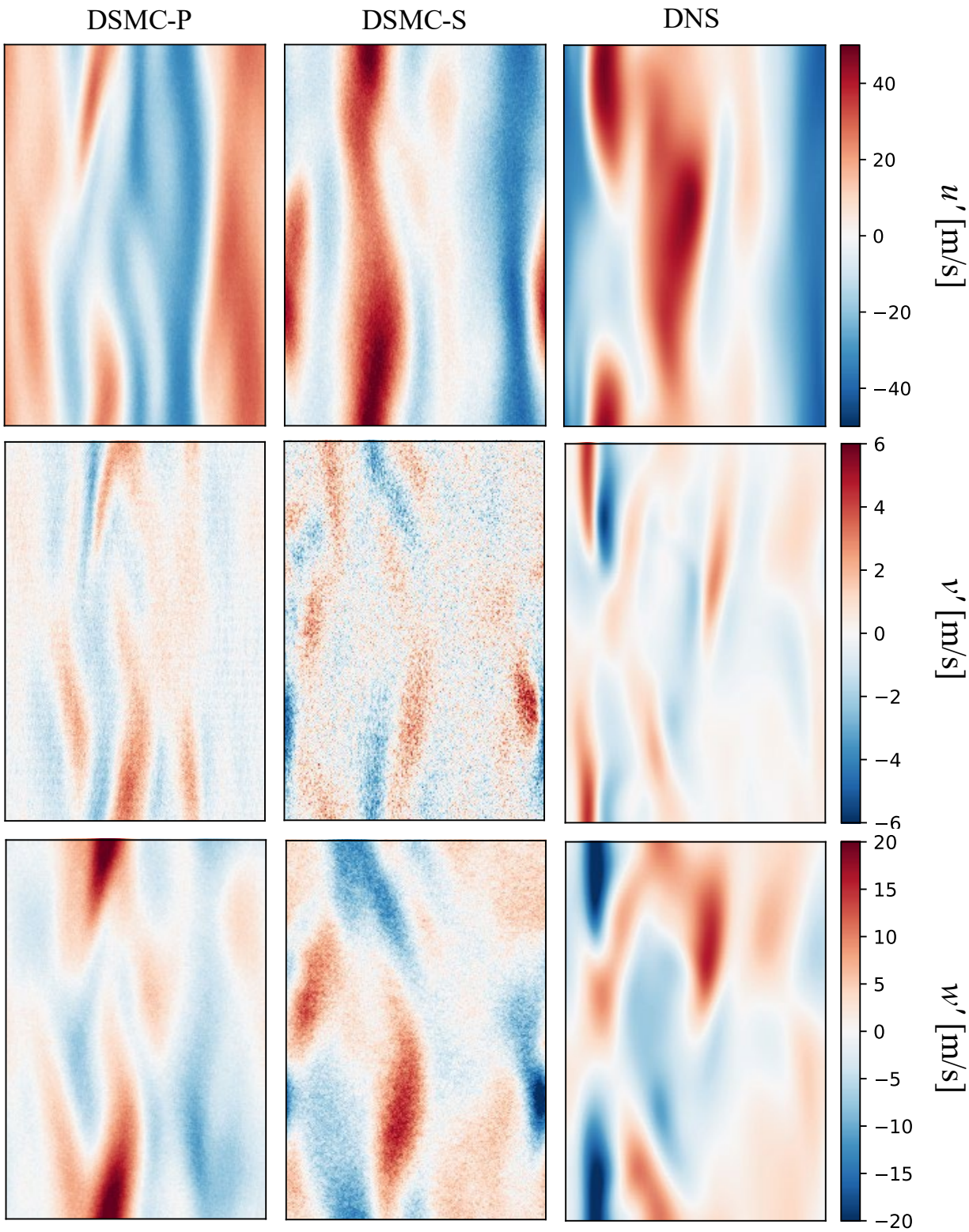

Fig. 11. Comparison of velocity fluctuations for $\mathrm{Re} = 1000$ at $y^+ = 5$. Left column: permeable-wall DSMC, center row: smooth-wall DSMC, right column: smooth-wall DNS. Top row: u, center row: v, bottom row: w. Images in the same row have the same color scale.

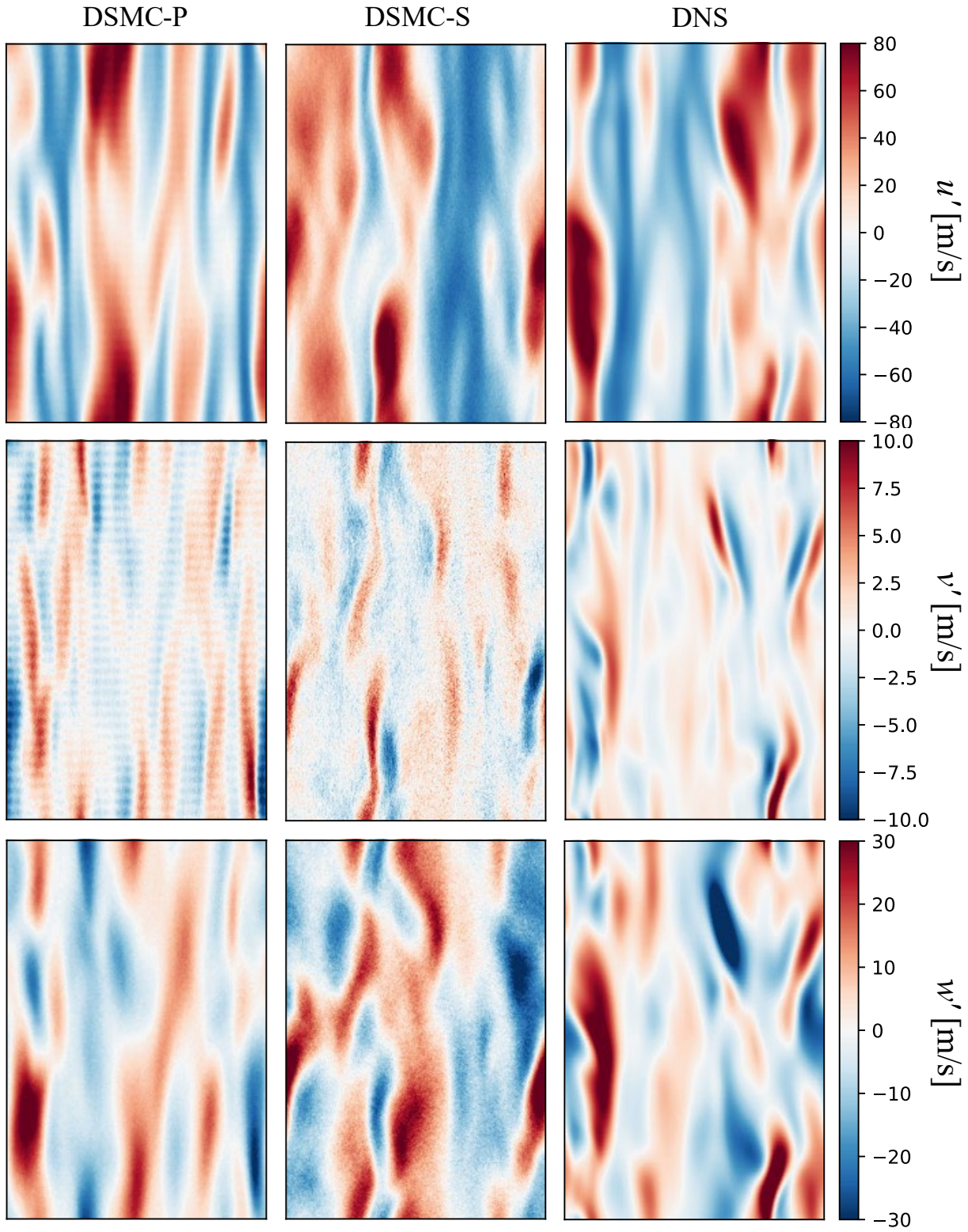

Fig. 12. Comparison of velocity fluctuations for $\mathrm{Re} = 1500$ at $y^+ = 5$. Left column: permeable-wall DSMC, center row: smooth-wall DSMC, right column: smooth-wall DNS. Top row: u, center row: v, bottom row: w. Images in the same row have the same color scale.

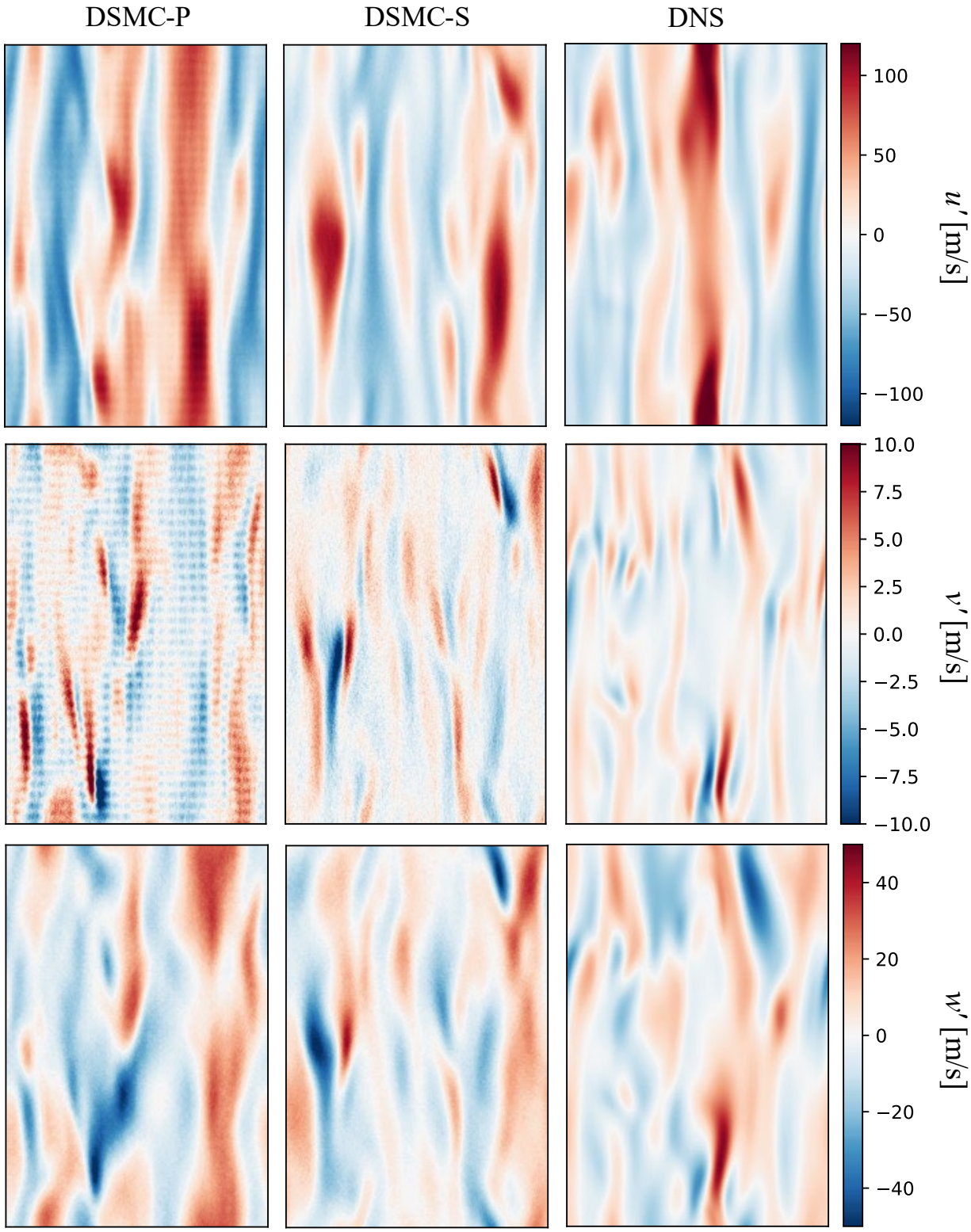

Fig. 13. Comparison of velocity fluctuations for $\mathrm{Re} = 2000$ at $y^+ = 5$. Left column: permeable-wall DSMC, center row: smooth-wall DSMC, right column: smooth-wall DNS. Top row: u, center row: v, bottom row: w. Images in the same row have the same color scale.

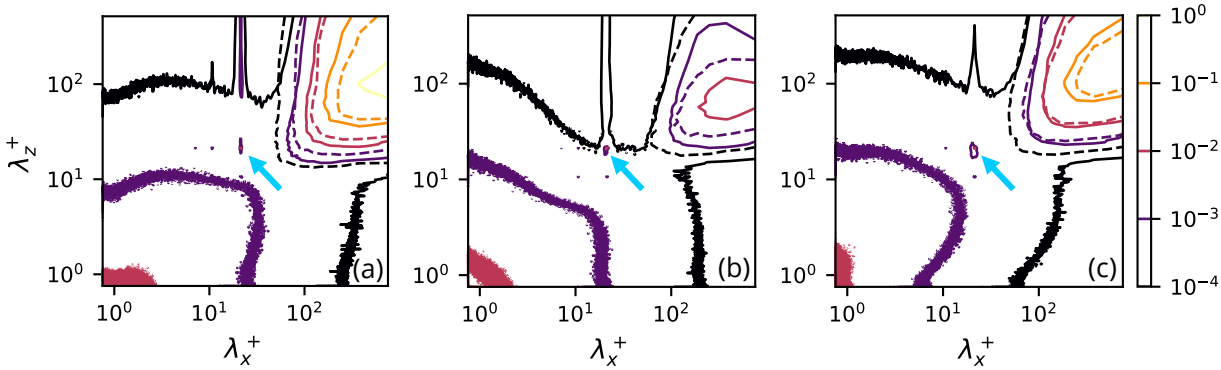

Fig. 14. Premultiplied energy spectra for $\mathrm{Re} = 2000$ at $y^+ = 5$. a) $k_x k_z E_{uu} / u_\tau^{l2}$, b) $k_x k_z E_{vv} / u_\tau^{l2}$, c) $k_x k_z E_{ww} / u_\tau^{l2}$. Solid lines are the permeable-wall DSMC. Dashed lines are the DNS. The cyan arrows indicate the peak corresponding to the cylinder spacing wavelength $\lambda_x^+ = \lambda_z^+ = 21.4$.

Table 3. Roughness, permeability, and noncontinuum parameters from the permeable-wall DSMC simulations.

Case	h/d	d^+	Re_K	Kn_s	λ^+
DSMC-P500	270	0.15	0.20	0.26	0.038
DSMC-P1000		0.25	0.35	0.25	0.062
DSMC-P1500		0.37	0.51	0.23	0.085
DSMC-P2000		0.51	0.70	0.21	0.106

IV. DISCUSSION

In this section, we discuss the results presented in Section III in the contexts of the literatures on rough-wall turbulence, permeable-wall turbulence, and noncontinuum flows.

A. Roughness effects

Real permeable substrates are frequently also hydrodynamically rough. Consequently, roughness-induced effects must be assessed along with permeability effects. Since the flow modifications induced by rough and permeable surfaces can present themselves in a similar manner [44,60], disentangling the two effects can be challenging.

Typically, the primary goal of studies of turbulent flow over rough surfaces is to establish a correlation between geometric properties of the roughness, principally a representative roughness height d, and the drag penalty associated with that surface [4-6]. However, standard tools for doing so rely on the Reynolds number being sufficiently high and the domain being sufficiently large [64] for the mean velocity profile to have a well-developed logarithmic region. This is clearly not the case for any of the profiles shown in Fig. 6. Consequently, we resort here to an indirect assessment of roughness effects.

First, as demonstrated in Fig. 3, there is a negligible drag increase on the cylinder structure relative to the smooth-wall shear stress, suggesting that the flow falls either in the hydraulically smooth or, at most, near the onset of the transitionally rough regime [4]. Next, we use the reasonable upper bound $d = s + r$ and lower bound $d = s$ on the roughness height (see Fig. 1) to obtain bounding blockage ratio estimates of $h/d = 24$ and 270, respectively. Classically, values of $h/d \lesssim 40$, are associated with the loss of outer-layer similarity, in which case roughness effects extend across much of the boundary layer, and the flow is more appropriately described as flow over obstacles [4].

By contrast, the smooth-wall near-wall dynamics are observed herein to be minimally affected by the presence of the cylinder structure (see Figs. 9-14), which motivates the use of $d = s$ as the representative roughness height. Therefore, this value is used for the values of h/d quoted in Table 3.

Also provided in Table 3 are values of the roughness Reynolds number d^+, which is smaller than unity for all cases. This suggests that the effects of the roughness are indeed limited to within a few viscous lengths above the cylinder structure. Therefore, we conclude that the modifications to the turbulent flow observed herein are primarily due to the permeability of the cylinder structure and that roughness has only a second-order effect on the flow.

B. Permeability effects

The permeability Reynolds number $\mathrm{Re}_K = \rho^l u_\tau^l K^{1/2} / \mu_w$, where K is the permeability, has been shown to be the dominant parameter describing the effects of a permeable wall [65]. For low-Re continuum flows, Darcy's law establishes the intrinsic permeability K_0 as a geometric property of the permeable material. However, rarefaction effects produce the well-known Klinkenberg effect [40], where the measured or apparent permeability K_a is larger than K_0 due to the relaxation of the no-slip condition [3,24]. Although the global Knudsen number Kn_h is small, this is not necessarily representative of the flow within the cylinder structure. Taking instead the cylinder spacing s as the characteristic length scale gives a pore-scale Knudsen number $\mathrm{Kn}_s = \lambda / s \approx 0.2$ (see Table 3), which is large enough that significant departures from the no-slip boundary condition may occur [14].

As shown in Table 3, Kn_s, and hence K_a, varies between the different Re cases. Therefore, Darcy-type DSMC simulations representative of the $\mathrm{Re} = 500$ and $\mathrm{Re} = 2000$ cases were performed to determine the maximum and minimum values of K_a, respectively. For these simulations, flow through a unit cell of the periodic cylinder structure was driven by a constant body force, the magnitude of which was selected to produce a flow velocity on the order of the velocity in the top layer of the cylinder structure (see Fig. 8). The mean pressure within the unit cell was selected to match the pressure within the cylinder structure in the Couette simulations. Darcy's law was then used to calculate K_a from the resulting mass flow rate, giving the values $K_a = 6.78\times10^{-12}\ \mathrm{m}^2$ and $K_a = 6.48\times10^{-12}\ \mathrm{m}^2$ for the $\mathrm{Re} = 500$ and $\mathrm{Re} = 2000$ cases, respectively. As stated above, these values represent the maximum and minimum values of K_a, indicating that the variation between all cases considered herein is small. Therefore, we use the mean value $\overline{K}_a = 6.63\times10^{-12}\ \mathrm{m}^2$ for all cases. Doing so introduces a negligible error ($\lesssim 1\%$) in the values of $\mathrm{Re}_K \sim K_a^{1/2}$ quoted in Table 3. For comparison, we additionally performed continuum simulations of Stokes flow for the same unit cell using the COMSOL Multiphysics® software package [66] to calculate the intrinsic permeability value $K_0 = 5.85\times10^{-12}\ \mathrm{m}^2$. Therefore, rarefaction results in a significant increase of $\approx 13\%$ in the apparent permeability of the cylinder structure, which should be accounted for to accurately determine Re_K.

Breugem et al. [48] classified the permeability of permeable substrates using Re_K. Surfaces for which $\mathrm{Re}_K \ll 1$ are said to be effectively impermeable, while surfaces for which $\mathrm{Re}_K \gg 1$ are said to be highly permeable. Finally, surfaces with $\mathrm{Re}_K \sim 1$ are partially permeable or transitional [10]. As the name suggests, the flow over an effectively impermeable surface is essentially unchanged from the flow over an impermeable wall. On the other hand, the near-wall streaks and vortices of impermeable-wall turbulence are completely absent in the highly permeable regime and are instead replaced by spanwise-coherent structures arising from a Kelvin-Helmholtz-type (K-H) instability of the mean velocity profile [48,51,54,56,60-62,67]. To characterize the onset of these structures in anisotropic permeable media, Gómez-de-Segura et al. [62] developed an empirical correlation for the parameter K_{Br}^+:

$$K_{\mathrm{Br}}^+ = K_y^+ \tanh\left(\frac{\sqrt{2K_x^+}}{9}\right)\tanh^2\left(\frac{h_c^+}{\sqrt{12K_y^+}}\right)$$

where K_x^+ and K_y^+ are the inner-scaled streamwise and wall-normal permeabilities, respectively. Using DNS, Gómez-de-Segura and García-Mayoral [61] found that the onset of K-H roller structures occurs when $\sqrt{K_{\mathrm{Br}}^+} \approx 0.4$. Since the present cylinder structure is isotropic, we use $\sqrt{K_x^+} = \sqrt{K_y^+} = \mathrm{Re}_K$ in the above. For the largest value of the

permeability Reynolds number, $\mathrm{Re}_K = 0.7$, corresponding to the $\mathrm{Re} = 2000$ case, we obtain $\sqrt{K_{\mathrm{Br}}^+} \approx 0.2$, which predicts that K-H-type structures will not be present, consistent with the fact that the only structures we observe with large spanwise coherence are those associated with the interface flow within the top layer of cylinders (see Figs. 11-14).

C. Noncontinuum effects in the free portion of the channel

Despite the fact that the local Knudsen number based on the viscous length scale $\lambda^+ = \rho^l u_\tau^l \lambda / \mu_w$ is as large as $O(10^{-1})$ for the simulations considered herein (see Table 3) and, therefore, approaches the regime where the continuum assumption breaks down [14], significant differences between the smooth-wall DSMC and DNS are not observed for the statistics and flow structures examined herein, suggesting that noncontinuum effects play a relatively minor role in the free portion of the channel.

This somewhat surprising observation raises the question of how large the Knudsen number needs to be to observe significant deviations from continuum behavior, or, further, at what value of the Knudsen number wall-bounded turbulence fails to self-sustain. Such a critical value must exist since the high-Knudsen-number limit is free-molecular flow, which cannot support turbulence. This question also has practical significance in the context of reentry vehicles, where the Knudsen number may vary by orders of magnitude over the course of their trajectories [68]. As a starting point, one would expect that the near-wall dynamics will change significantly when the Knudsen layer thickness becomes comparable to the viscous length scale. Because the Knudsen layer is $O(\lambda)$ [14], this condition can be expressed as $\lambda^+ \sim 1$. Since $\lambda^+ = \sqrt{\pi\gamma/2}\,\mathrm{Ma}_\tau$, where $\mathrm{Ma}_\tau = u_\tau / a$, $\lambda^+ \sim 1$ implies $\mathrm{Ma}_\tau \sim \sqrt{2/\pi\gamma} \approx 0.6$, which would require a substantially larger global Mach number. We emphasize that this is only a rough estimate but note that such large Mach numbers may not be unrealistic in the context of reentry vehicles [69]. Exploring such a regime is an avenue for future work.

V. CONCLUSIONS

The present paper presents an investigation of turbulent Couette flow in a minimal domain over a mean-free-path-scale permeable surface using DSMC simulations. Four different Reynolds numbers are considered. In order to assess the impact of the surface on the turbulence, comparisons are made to smooth-wall Couette flow simulated with both DSMC and DNS of the Navier-Stokes equations for the same conditions.

Comparisons of the shear stress on the upper wall show good agreement between all three simulations, indicating that the permeable substrate considered herein does not have a significant impact on drag.

The mean velocity profiles demonstrate that for the lower-Reynolds-number cases considered, the primary modification to the mean flow is the presence of a finite slip velocity at the interface of the cylinder structure. This interface slip velocity is approximately constant when scaled by $\tau^l h / \mu_w$ over the range of Re_τ^l considered herein. This scaling is distinct from scaling observed in higher-Reynolds-number flows [44,48-50] and may indicate a transition from viscous-dominated to pressure-dominated drag at an intermediate Reynolds number. The mean flow within the top two layers of the structure shows the signature of recirculation vortices, as are often found in flows over *d*-type roughness [51,52]. The velocity profiles within the second layer are found to collapse when scaled by $\tau^l h / \mu_w$, though this scaling does not completely collapse the profiles in the first layer.

Representative snapshots of near-wall velocity fluctuations in the plane $y^+ = 5$ indicate that the presence of the cylinder structure does not significantly alter the near-wall structures. However, the cylinder structure clearly modulates the velocity fluctuations for all cases, except the lowest Reynolds number, $\mathrm{Re} = 500$. The velocity spectra in the same wall-normal plane confirm these observations and show the signature of spanwise coherence across the entire domain with a wavelength corresponding to the spacing between the vertical cylinders.

Rarefaction effects within the cylinder structure result in a significant increase in its apparent permeability relative to the intrinsic permeability. By contrast, rarefaction effects in the free portion of the channel were found to have negligible impact on the flow statistics, despite the viscous Knudsen number λ^+ being $O(10^{-1})$, which is at variance with classical estimates for the breakdown of the continuum assumption [14]. This highlights the need for further fundamental understanding of the interaction between noncontinuum effects and turbulence.

Finally, we have demonstrated the ability of DSMC to simulate turbulent flows over complex geometries, including those having characteristic length scales of the order of the mean free path, which are relevant for flow over TPS materials. To the best of our knowledge, this is the first time noncontinuum effects have been considered for

turbulent flow over a permeable wall. Despite the computationally intensive nature of DSMC, its unique capabilities enable future studies of turbulent flow over TPS materials in regimes featuring strong noncontinuum and thermochemical nonequilibrium effects. Future work will consider the additional effects of surface chemistry and ablation on the overlying turbulent flow.

APPENDIX A: TURBULENT MACH NUMBER

Fig. 15 shows profiles of the turbulent Mach number $\mathrm{Ma}_t = u_{\mathrm{rms}} / \bar{a}$, where $u_{\mathrm{rms}} = \sqrt{\overline{u'^2} + \overline{v'^2} + \overline{w'^2}}$ is the rms fluctuating velocity and $\bar{a}$ is the mean sound speed, for all DNS cases. The peak values corresponding to the $\mathrm{Re} = 500,\ 1000,\ 1500,\ 2000$ cases are $\mathrm{Ma}_{t,\max} = 0.0829,\ 0.140,\ 0.176,\ 0.219$, respectively.

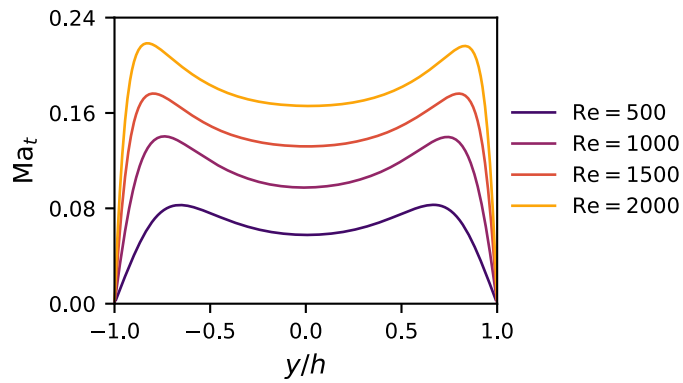

Fig. 15. Turbulent Mach number profiles from the DNS.

APPENDIX B: INITIAL TRANSIENTS WITHIN THE CYLINDER STRUCTURE

Here, we show that transients within the cylinder structure due to the initial condition decay sufficiently rapidly such that the flow reaches statistically steady state by $tU_w / h = 200$, after which samples are collected for time-averaged statistics. Fig. 16 compares spatially averaged density profiles at early times ($tU_w / h \leq 12$) with profiles near the beginning of the steady state ($tU_w / h \approx 200$). The early-time profiles clearly show remnants of the initial condition, with strong asymmetry across the channel and nonuniform density within the cylinder structure (left of the black dashed line). By contrast, the profiles corresponding to $tU_w / h \approx 200$ have uniform density within the cylinder

structure and are nearly identical to the temporally averaged profiles in all cases. This, along with the skin friction plots shown in Figs. 2 and 3, confirm that the flow reaches steady state by $tU_w / h = 200$.

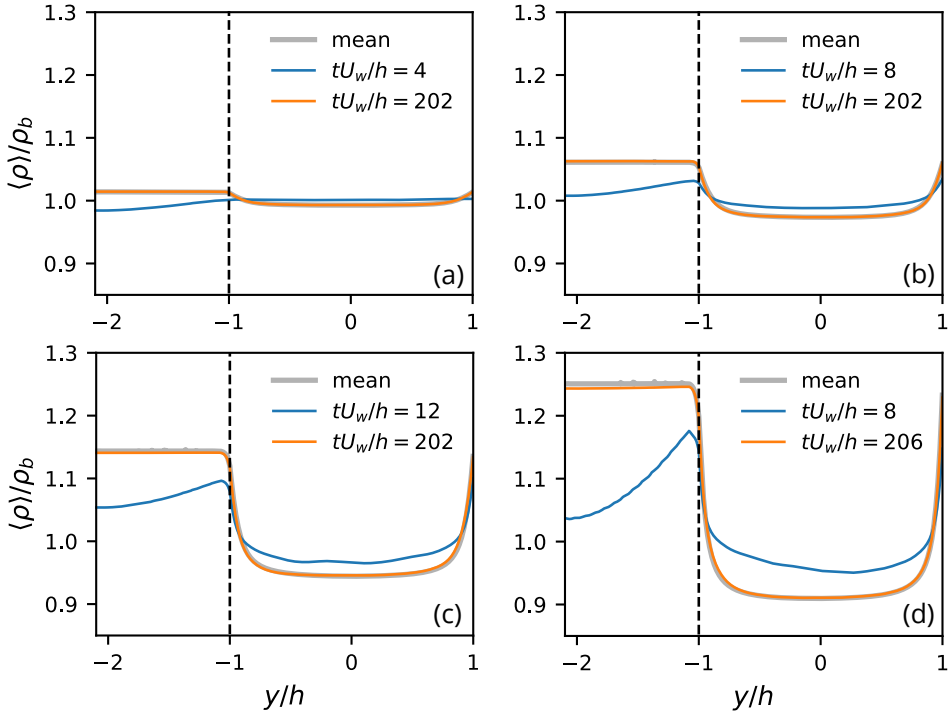

Fig. 16. Comparison of early-time (blue lines), steady-state (orange lines), and temporal mean (gray lines) spatially averaged density profiles normalized by the bulk density ρ_b. (a) Re = 500, (b) Re = 1000, (c) Re = 1500, (d) Re = 2000. The vertical black dashed line indicates the location of the top of the cylinder structure.

ACKNOWLEDGMENTS

This article has been authored by an employee of National Technology & Engineering Solutions of Sandia, LLC under Contract No. DE-NA0003525 with the U.S. Department of Energy (DOE). The employee owns all right, title and interest in and to the article and is solely responsible for its contents. The United States Government retains and the publisher, by accepting the article for publication, acknowledges that the United States Government retains a non-exclusive, paid-up, irrevocable, world-wide license to publish or reproduce the published form of this article or allow others to do so, for United States Government purposes. The DOE will provide public access to these results of federally sponsored research in accordance with the DOE Public Access Plan https://www.energy.gov/downloads/doe-public-access-plan.

The authors thank Dr. T. P. Koehler of Sandia National Laboratories for creating the cylinder structure geometry and Drs. L. J. DeChant and M. Barone of Sandia National Laboratories for helpful discussions about this work.

[1] O. Uyanna and H. Najafi, Thermal protection systems for space vehicles: A review on technology development, current challenges and future prospects, Acta Astro. **176**, 341 (2020).
[2] E. C. Stern, S. J. Poovathingal, I. Nompelis, T. E. Schwartzentruber, and G. V. Candler, Nonequilibrium flow thorugh porous thermal portection materials, Part I: Numerical methods, J. Comp. Phys. **380**, 408 (2019).
[3] S. J. Poovathingal, E. C. Stern, I. Nompelis, T. E. Schwartzentruber, and G. V. Candler, Nonequilibrium flow thorugh porous thermal portection materials, Part II: Oxidation and pyrolysis, J. Comp. Phys. **380**, 427 (2019).
[4] J. Jiménez, Turbulent flows over rough walls, Annu. Rev. Fluid Mech. **36**, 173 (2004).
[5] K. A. Flack and M. P. Schultz, Roughness effects on wall-bounded turbulent flows, Phys. Fluids **26**, 101305 (2014).
[6] D. Chung, N. Hutchins, M. P. Schultz, and K. A. Flack, Predicting the drag of rough surfaces, Annu. Rev. Fluid Mech. **53**, 439 (2021).

[7] J. Finnigan, Turbulence in plant canopies, Annu. Rev. Fluid Mech. **32**, 519 (2000).
[8] M. Chandesris, A. D'Hueppe, B. Mathieu, D. Jamet, and B. Goyeau, Direct numerical simulation of turbulent heat transfer in a fluid-porous domain, Phys. Fluids **25**, 125110 (2013).
[9] Y. A. Hassan and E. E. Dominguez-Ontiveros, Flow visualization in a pebble bed reactor experiment using PIV and refractive index matching techniques, Nuc. Eng. Des. **238**, 3080 (2008).
[10] J. J. Voermans, M. Ghisalberti, and G. N. Ivey, The variation of flow and turbulence across the sediment-water interface, J. Fluid Mech. **824**, 413 (2017).
[11] M. R. Raupach, J. J. Finnigan, and Y. Brunet, Coherent eddies and turbulence in vegetation canopies: the mixing-layer analogy, Boundary-Layer Meteorol. **78**, 351 (1996).
[12] E. C. Stern, I. Nompelis, T. E. Schwartzentruber, and G. V. Candler, Microscale Simulations of Porous TPS Materials: Application to Permeability, 2014-2247 (American Institute of Aeronautics and Astronautics, Atlanta, GA, 2014).
[13] M. A. Gallis, J. R. Torczynski, N. P. Bitter, T. P. Koehler, S. J. Plimpton, and G. Papadakis, Gas-kinetic simulation of sustained turbulence in minimal Couette flow, Phys. Rev. Fluids **3**, 071402 (2018).
[14] G. A. Bird, *Molecular Gas Dynamics and the Direct Simulation of Gas Flows* (Clarendon Press, Oxford, 1994).
[15] M. A. Gallis, N. P. Bitter, T. P. Koehler, J. R. Torczynski, S. J. Plimpton, and G. Papadakis, Molecular-level simulations of turbulence and its decay, Phys. Rev. Lett. **118**, 064501 (2017).
[16] M. A. Gallis, J. R. Torczynski, M. C. Krygier, N. P. Bitter, and S. J. Plimpton, Turbulence at the edge of continuum, Phys. Rev. Fluids **6**, 013401 (2021).
[17] R. M. McMullen, M. C. Krygier, J. R. Torczynski, and M. A. Gallis, Navier-Stokes equations do not describe the smallest scales of turbulence in gases, Phys. Rev. Lett. **128**, 114501 (2022).
[18] D. Bandak, N. Goldenfeld, A. A. Mailybaev, and G. Eyink, Dissipation-range fluid turbulence and thermal noise, Phys. Rev. E **105**, 065113 (2022).
[19] J. B. Bell, A. Nonaka, A. L. Garcia, and G. Eyink, Thermal fluctuations in the dissipation range of homogeneous Isotropic turbulence, J. Fluid Mech. **939**, A12 (2022).
[20] R. M. McMullen, J. R. Torczynski, and M. A. Gallis, Thermal-fluctuation effects on small-scale statistics in turbulent gas flow, Phys. Fluids **35**, 011705 (2023).
[21] J. M. Hamilton, J. Kim, and F. Waleffe, Regeneration mechanisms of near-wall turbulence structures, J. Fluid Mech. **287**, 317 (1995).
[22] S. S. Sawant, A. Harpale, R. Jambunathan, H. B. Chew, and D. A. Levin, High Fidelity and Multi-Scale Thermal Response Modeling of an Avcoat-like Thermal Protection System Material, AIAA-2017-0438 (American Institute of Aeronautics and Astronautics, Grapevine, TX, 2017).
[23] R. Jambunathan, D. A. Levin, A. Borner, J. C. Ferguson, and F. Panerai, Prediction of gas transport properties through fibrous carbon preform microstructures using Direct Simulation Monte Carlo, Int. J. Heat Mass Tran. **130**, 923 (2019).
[24] S. J. Poovathingal, B. M. Soto, and C. Brewer, Effective Permeability of Carbon Composites Under Reentry Conditions, AIAA J. **60**, 1293 (2022).
[25] S. J. Plimpton, S. G. Moore, A. Borner, A. K. Stagg, T. P. Koehler, J. R. Torczynski, and M. A. Gallis, Direct simulation Monte Carlo on petaflop supercomputers and beyond, Phys. Fluids **31**, 086101 (2019).
[26] M. A. Gallis, Koehler, T. P., and Plimpton, S. J., SPARTA Stochastic Particle Real Time Analyzer Validation and Verification Test Suite, Report No. SAND2014-19198, 2014.
[27] H. A. Al-Mohssen and N. G. Hadjiconstantinou, Low-variance Monte Carlo simulations using importance weights, ESIAM Math. Model. Numer. Anal., 1069 (2010).
[28] M. Sadr and N. G. Hadjiconstantinou, A variance-reduced direct Monte Carlo simulation method for solving the Boltzmann equation over a wide range of rarefaction, J. Comp. Phys. **472**, 111677 (2023).
[29] M. Howard, A. Bradley, S. W. Bova, J. Overfelt, R. Wagnild, D. Dinzl, M. Hoemmen, and A. Klinvex, Towards performance portability in a compressible CFD code, AIAA-2017-4407 (American Institute of Aeronautics and Astronautics, Reston, VA, 2017).
[30] P. K. Subbareddy and G. V. Candler, A fully discrete, kinetic energy consistent finite-volume scheme for compressible flows, J. Comp. Phys. **228**, 1347 (2009).
[31] R. W. MacCormack and G. V. Candler, The solution of the Navier-Stokes equations using Gauss-Seidel line relaxation, Comput. Fluids **17**, 135 (1989).
[32] D. Modesti and S. Pirozzoli, Reynolds and Mach number effects in compressible turbulent channel flow, Int. J. Heat Fluid Flow **59**, 33 (2016).
[33] M. Yu, C.-X. Xu, and S. Pirozzoli, Genuine compressibility effects in wall-bounded turbulence, Phys. Rev. Fluids **4**, 123402 (2019).
[34] J. Yao and F. Hussain, Turbulence statistics and coherent structures in compressible channel flow, Phys. Rev. Fluids **5**, 084603 (2020).

[35] T. Szemberg O'Connor, PhD Thesis, Imperial College London (2018).
[36] P. E. S. Chen, Y. Lv, H. H. A. Xu, Y. Shi, and X. I. A. Yang, LES wall modeling for heat transfer at high speeds, Phys. Rev. Fluids **7**, 014608 (2022).
[37] J. Yao and F. Hussain, Study of compressible turbulent plane Couette flows via direct numerical simulation, J. Fluid Mech. **964**, A29 (2023).
[38] J. C. Buell, Direct simulations of compressible wall-bounded turbulence, 1991.
[39] C. Lowery, R. Ranjan, and V. Hasti, Characteristics of Non-Equilibrium Turbulence in Couette Flow under Compressible Conditions, 2022-4035 (American Institute of Aeronautics and Astronautics, Chicago, IL, 2022).
[40] L. J. Klinkenberg, The permeability of porous media to liquids and gases, Am. Petrol. Inst. **2**, 200 (1941).
[41] L. Wu, M. T. Ho, L. Germanou, X.-J. Gu, C. Liu, K. Xu, and Y. Zhang, On the apparent permeability of porous media in rarefied gas flows, J. Fluid Mech. **822**, 398 (2017).
[42] A. J. Smits and J. P. Dussauge, *Turbulent Shear Layers in Supersonic Flow* (Springer, Berlin, 2006).
[43] T. M. Schneider, F. De Lillo, J. Buehrle, B. Eckhardt, T. Dornemann, K. Dornemann, and B. Freisleben, Transient turbulence in plane Couette flow, Phys. Rev. E **81**, 015301(R) (2010).
[44] L. B. Esteban, E. Rodríguez-López, M. A. Ferreira, and B. Ganapathisubramani, Mean flow of turbulent boundary layers over porous substrates, Phys. Rev. Fluids **7**, 094603 (2022).
[45] M. Lee and R. D. Moser, Extreme-scale motions in turbulent plane Couette flows, J. Fluid Mech. **842**, 128 (2018).
[46] F. Waleffe, On a self-sustaining process in shear flows, Phys. Fluids **9**, 883 (1997).
[47] S. Pirozzoli, M. Bernardini, and P. Orlandi, Turbulence statistics in Couette flow at high Reynolds number, J. Fluid Mech. **758**, 327 (2014).
[48] W. Breugem, B. Boersma, and R. Uittenbogaard, The influence of wall permeability on turbulent channel flow, J. Fluid Mech. **562**, 35 (2006).
[49] C. Efstathiou and M. Luhar, Mean turbulence statistics in boundary layers over high-porosity foams, J. Fluid Mech. **841**, 351 (2018).
[50] K. Suga, Y. Matsumura, Y. Ashitaka, S. Tominaga, and M. Kaneda, Effects of wall permeability on turbulence, Int. J. Heat Fluid Flow **31**, 974 (2010).
[51] Y. Kuwata and K. Suga, Direct numerical simulation of turbulence over anisotropic porous media, J. Fluid Mech. **831**, 41 (2017).
[52] A. E. Perry, W. H. Schofield, and P. N. Joubert, Rough wall turbulent boundary layers, J. Fluid Mech. **37**, 383 (1969).
[53] S. K. Javanappa and V. D. Narasimhamurthy, Turbulent plane Couette flow with a roughened wall, Phys. Rev. Fluids **6**, 104609 (2021).
[54] J. Jiménez, M. Uhlmann, A. Pinelli, and G. Kawahara, Turbulent shear flow over active and passive porous surfaces, J. Fluid Mech. **442**, 89 (2001).
[55] C. Manes, D. Poggi, and L. Ridolfi, Turbulent boundary layers over permeable walls: scaling and near-wall structure, J. Fluid Mech. **687**, 141 (2011).
[56] S. M. Habibi Khorasani, M. Luhar, and S. Bagheri, Turbulent flows over engineered anisotropic porous substrates, arXiv:2210.10140 (2022).
[57] R. García-Mayoral and J. Jiménez, Hydrodynamic stability and breakdown of the viscous regime over riblets, J. Fluid Mech. **678**, 317 (2011).
[58] A. Chavarin and M. Luhar, Resolvent Analysis for Turbulent Channel Flow with Riblets, AIAA J. **58**, 589 (2020).
[59] S. Toedtli, C. Yu, and B. McKeon, On the origin of drag increase in varying-phase opposition control, Int. J. Heat Fluid Flow **85**, 108651 (2020).
[60] Y. Kuwata and K. Suga, Lattice Boltzmann direct numerical simulation of interface turbulence over porous and rough walls, Int. J. Heat Fluid Flow **61**, 145 (2016).
[61] G. Gómez-de-Segura and R. García-Mayoral, Turbulent drag reduction by anisotropic permeable substrates - analysis and direct numerical simulations, J. Fluid Mech. **875**, 124 (2019).
[62] G. Gómez-de-Segura, A. Sharma, and R. García-Mayoral, Turbulent drag reduction using anisotropic permeable substrates, Flow, Turbul. Combust. **100**, 995 (2018).
[63] A. Chavarin, C. Efstathiou, S. Vijay, and M. Luhar, Resolvent-based design and experimental testing of porous materials for passive turbulence control, Int. J. Heat Fluid Flow **86**, 108722 (2020).
[64] D. Chung, L. Chan, M. MacDonald, N. Hutchins, and A. Ooi, A fast direct numerical simulation method for characterising hydraulic roughness, J. Fluid Mech. **773**, 418 (2015).
[65] M. E. Rosti, L. Cortelezzi, and M. Quadrio, Direct numerical simulation of turbulent channel flow over porous walls, J. Fluid Mech. **784**, 396 (2015).
[66] COMSOL Multiphysics® v. 6.1, COMSOL AB, 2022.

[67] N. Abderrahaman-Elena and R. García-Mayoral, Analysis of anisotropically permeable surfaces for turbulent drag reduction, Phys. Rev. Fluids **2**, 114609 (2017).
[68] J. Lachaud, I. Cozmuta, and N. N. Mansour, Multiscale Approach to Ablation Modeling of Phenolic Impregnated Carbon Ablators, J. Spacecraft Rockets **47**, 910 (2010).
[69] G. V. Candler, Rate Effects in Hypersonic Flows, Annu. Rev. Fluid Mech. **51**, 379 (2019).